Molecular Therapy
Oncolytics
Original Article

Preclinical assessment of a novel human antibody VH domain targeting mesothelin as an antibody-drug conjugate

Zehua Sun,[1,4] Xiaojie Chu,[1,4] Cynthia Adams,[2,4] Tatiana V. Ilina,[3] Michel Guerrero,[3] Guowu Lin,[3] Chuan Chen,[1] Dontcho Jelev,[1] Rieko Ishima,[3] Wei Li,[1] John W. Mellors,[1,2] Guillermo Calero,[3] and Dimiter S. Dimitrov[1,2]

[1]Center for Antibody Therapeutics, Division of Infectious Diseases, Department of Medicine, University of Pittsburgh School of Medicine, 3550 Terrace Street, Pittsburgh, PA 15261, USA; [2]Abound Bio, 1401 Forbes Avenue, Pittsburgh, PA 15219, USA; [3]Department of Structural Biology, University of Pittsburgh School of Medicine, 3501 Fifth Avenue, Pittsburgh, PA 15260, USA

Mesothelin (MSLN) has been a validated tumor-associated antigen target for several solid tumors for over a decade, making it an attractive option for therapeutic interventions. Novel antibodies with high affinity and better therapeutic properties are needed. In the current study, we have isolated and characterized a novel heavy chain variable (VH) domain 3C9 from a large-size human immunoglobulin VH domain library. 3C9 exhibited high affinity (KD [dissociation constant] <3 nM) and binding specificity in a membrane proteome array (MPA). In a mouse xenograft model, 3C9 fused to human IgG1 Fc was detected at tumor sites as early as 8 h post-infusion and remained at the site for over 10 days. Furthermore, 3C9 fused to a human Fc domain drug conjugate effectively inhibited MSLN-positive tumor growth in a mouse xenograft model. The X-ray crystal structure of full-length MSLN in complex with 3C9 reveals interaction of the 3C9 domains with two distinctive residue patches on the MSLN surface. This newly discovered VH antibody domain has a high potential as a therapeutic candidate for MSLN-expressing cancers.

INTRODUCTION

Mesothelin (MSLN) is an attractive tumor-associated antigen target for multiple solid tumors.[1–5] Several antibody-based therapeutics, including immunotoxins, chimeric antigen receptor T-cells (CAR-Ts), and antibody-drug conjugates (ADCs) have shown antitumor activity in clinical trials, and these existing therapeutics have offered important insights into the complexities of treating MSLN-expressing solid tumors, revealing areas that require further investigation.[6–8] There are several requirements for antibody-based therapeutics against MSLN-expressing solid tumors: (1) high antibody affinity and avidity allowing recognition of tumor cells with low surface density of MSLN; (2) improved antigen specificity to minimize off-target binding and related cytotoxicity; (3) better antibody penetration of solid tumors; and (4) reduced aggregation of the antibody. Addressing these issues is essential for the development of effective therapies against MSLN-expressing solid tumors. The development of novel antibodies with reasonable antigen specificity and suitable affinity may also help overcome these issues.

Since Food and Drug Administration (FDA) approval of the first VH antibody domain, caplacizumab, in 2019, VH antibody domains have gained attention for their potential advantages over traditional antibodies, especially their better penetration of solid tumors because of small size and reduced immunogenicity (fewer epitopes).[9–12] Several human VH antibody domains are being evaluated as CARs, monoclonal antibody (mAb) antagonists, or bispecific T cell engagers (biTEs).[13–15] Thus far, VH antibody domains targeting MSLN have not been reported in clinical development.

We previously constructed a high-quality and diverse human antibody VH domain library based on thermo-stable anti-aggregation scaffolds for phage display.[9] Using this library, we isolated a novel MSLN-specific antibody domain, 3C9, with high affinity (K_D [dissociation constant] <3 nM) and specificity. Specificity was confirmed through a human MPA of approximately 6,000 surface proteins, where no off-target binding was observed. In addition, the crystal structure of the full-length MSLN-3C9 complex was determined and revealed a unique binding site that distinguishes 3C9 from other MSLN binders, including those that have advanced to clinical development.[16] *In vivo* studies demonstrated the high specificity of 3C9 to

Received 1 March 2023; accepted 8 September 2023;
https://doi.org/10.1016/j.omto.2023.09.002.

[4]These authors contributed equally

Correspondence: Zehua Sun, PhD, Center for Antibody Therapeutics, Division of Infectious Diseases, Department of Medicine, University of Pittsburgh School of Medicine, 3550 Terrace Street, Pittsburgh, PA 15261, USA.
E-mail: zes20@pitt.edu
Correspondence: Guillermo Calero, PhD, Department of Structural Biology, University of Pittsburgh School of Medicine, 3501 Fifth Avenue, Pittsburgh, PA 15260, USA.
E-mail: guc9@pitt.edu
Correspondence: Dimiter S. Dimitrov, PhD, Center for Antibody Therapeutics, Division of Infectious Diseases, Department of Medicine, University of Pittsburgh School of Medicine, 3550 Terrace Street, Pittsburgh, PA 15261, USA.
E-mail: mit666666@pitt.edu

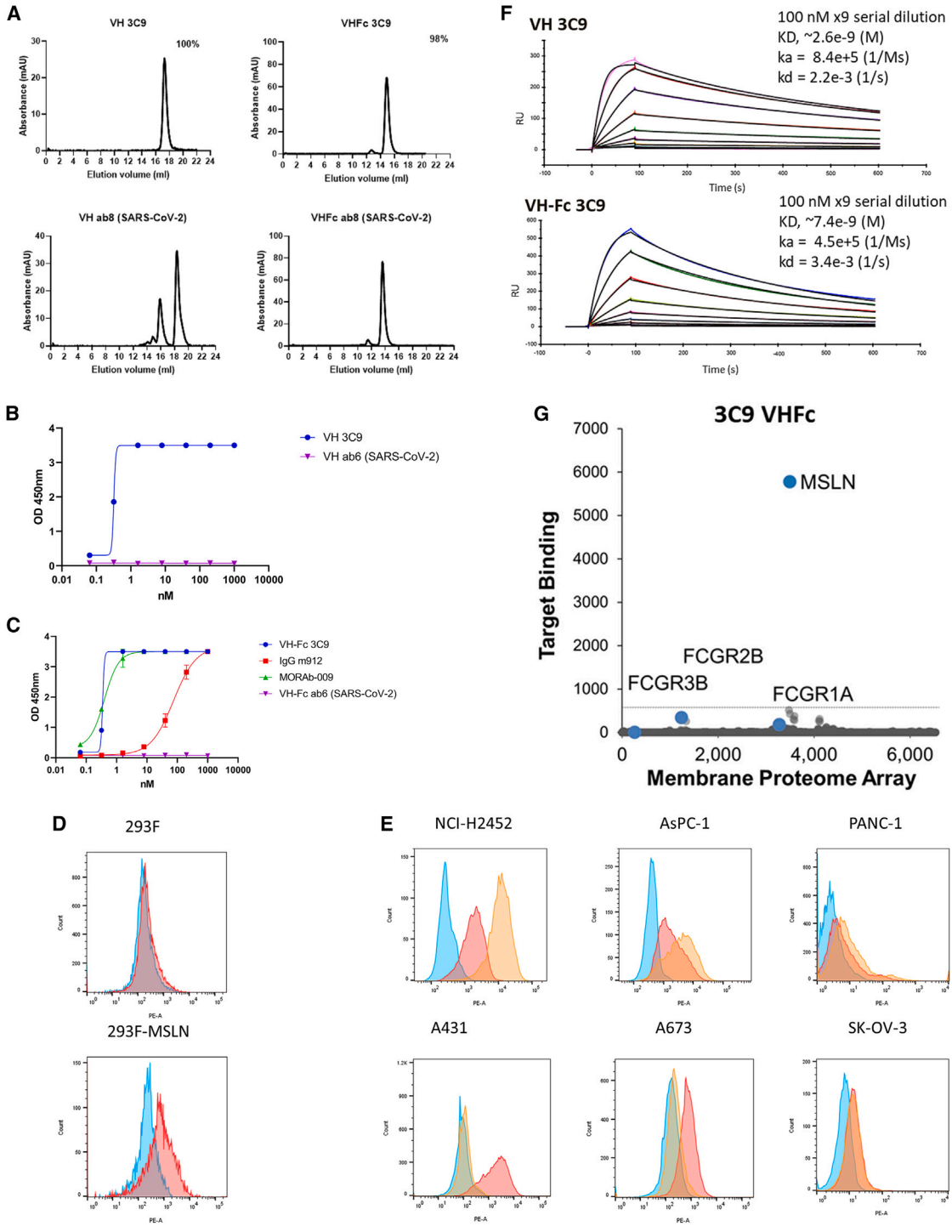

Figure 1. Characterization of 3C9

(A) SEC data of both VH and VH-Fc 3C9. Aggregation-resistant VH and VH-Fc ab8 were used as controls. (B and C) ELISA of VH/VH-Fc binders binding to human MSLN. (D) 3C9 did not show any binding to 293F cells, but it exhibited positive binding when tested on 293F cells that were transiently transfected with MSLN. 3C9 was labeled in red,

(legend continued on next page)

MSLN and its therapeutic potential as ADCs, supporting its further development as a therapeutic candidate for MSLN-expressing cancers.

RESULTS

Discovery and characterization of a novel human MSLN-specific VH antibody domain

We designed human recombinant MSLN constructs, which were expressed and used as antigens to isolate MSLN-specific binders from a large-size human antibody VH domain library by phage display.[9] This approach yielded a panel of unique domains with affinities ranging from 0.5 nM to 200 nM for human MSLN. We extensively characterized one VH domain, 3C9, with high affinity and favorable non-aggregation profile: 3C9 itself did not exhibit any dimer fraction in size-exclusion chromatography (SEC) (Figure 1A, left upper panel). In an ELISA assay, 3C9 exhibited a half maximal effective concentration (EC50) less than 10 nM (Figure 1B). Consistent with the ELISA observation, in a surface plasmon resonance (SPR) assay, 3C9 exhibited a high affinity to human MSLN with the KD less than 3 nM (Figure 1F, upper panel). VH 3C9 also binds macaque MSLN, though with a lower binding affinity (KD >100 nM, data not shown).

To measure the effect of avidity and to extend its half-life, the VH domain was fused with human immunoglobulin (Ig)G1 Fc protein to form proteins of a bivalent format (VH-Fc). VH-Fc proteins were purified from transfected Expi293 cells with yields ranging from 40–60 mg/L (Figure 1A, upper right panel). VH-Fc 3C9 had an EC50 of less than 1 nM (Figure 1C) by ELISA, which was comparable to MORAb-009, a mouse-human IgG1/k monoclonal antibody in Phase 2 clinical development.[8,17,18] By SPR assay, the KD of VH-Fc 3C9 was 7 nM (Figure 1F, lower panel). The reduced avidity is probably caused by the fixed orientations of VHs by the Fc protein.[12]

According to the reported data, 293F cells exhibited a negative binding to IL12-SS1 (Fv), suggesting a very low or no expression of MSLN on the cell surface.[19] In line with these findings, VH-Fc 3C9 did not show any binding to 293F cells; however, VH-Fc 3C9 showed positive binding when tested on 293F cells that were transiently transfected with MSLN (Figure 1D). Cell binding was further assessed by flow cytometry using VH-Fc 3C9 or mAb m912, which was previously shown to strongly bind to cells expressing MSLN.[20] Various cell types were employed for the binding studies, including two cell lines with high MSLN expression: pancreas adenocarcinoma (AsPC-1) and mesothelioma (NCI-H2452). Additionally, two cell lines with lower MSLN expression were used: epithelioid carcinomas (PANC-1) and ovarian adenocarcinomas (SK-OV-3). Two negative cell lines were included: epidermoid carcinoma (A-431) and Ewing's sarcoma (A-673). As expected, mAb m912 (shown in red) exhibited strong binding to NCI-H2452 and AsPC-1 cells, while demonstrating weaker binding to PANC-1 and SK-OV-3 cells. M912 also showed non-specific binding to negative cell lines A-431 and A-673. In contrast, VH-Fc 3C9 (shown in yellow) displayed reactivity with NCI-H2452, AsPC-1, PANC-1, and SK-OV-3 cells. Its binding activity at the same dose (50 nM) generally exceeded that of mAb m912. Notably, VH-Fc 3C9 did not exhibit any binding activity toward the negative cell lines A-431 and A-673 (Figure 1E). These data suggest the potential of VH-Fc 3C9 as a specific binder, although further characterization is required. These data indicate the specificity of VH-Fc 3C9.

A membrane proteome array (MPA) platform[21] was used to test specificities of VH-Fc 3C9 against a total 6,000 different human membrane proteins, including 94% of all single-pass, multi-pass, and GPI-anchored proteins (GPCRs, ion channels, and transporters). Cell-specific binding was first verified in a concentration-dependent manner and was validated before the MPA assay. VH-Fc 3C9 showed no off-target binding to 6,000 membrane-associated proteins tested (Figure 1G).

Structural basis of 3C9 binding to MSLN

Crystals of the SEC purified MSLN and 3C9 complex appeared under 0.18 M tri-ammonium citrate and 20% PEG 3350. Initial phases to 2.9 Å resolution were obtained by multiple anomalous diffraction of selenomethionyl labeled VH 3C9 (Figure 2). At this resolution, side chains were clearly visible, allowing residue placement, as described below. The model was subjected to several rounds of manual building in Coot64 and refinement using Phenix66 to a final R-free and R-work of 25% and 22%, respectively (Table 1). The asymmetric unit contains two MSLN molecules, each one interacting with two VH 3C9 molecules (Figures 2A, S1A, and S1B). The structure of the full mature MSLN (residues 300 to 592) comprises 10 alpha helical hairpins (helix-loop-helix) forming a super-helical solenoid (Figure S2A). An internal disulfide bond, C442-C468 (Figure S2A), between hairpins 5 and 6 confers rigidity to the solenoid. Calculation of the surface electrostatic potential shows the presence of charged pockets and crevices that could represent prospective interaction areas (Figure S2B). The MSLN fold is essentially the same as that published recently (Figure S2C).[16]

Two 3C9 molecules (heretofore VH_1 and VH_2) form a swapped dimer domain that features a significant contact area (burying 1805 $Å^2$) and 31 hydrogen bonds/salt bridges (Figures 2B, 2C, S3A, and S3B). These interactions comprise the CDR3 loops (residues 97–104); and the C-terminal strand of VH_1 (VH_2) completing the B-sheet of VH_2 (VH_1) (Table S1, interactions; Figures S3C and S3D).

while the isotype control was labeled in blue. (E) Individual cell lines were analyzed by flow cytometry after staining with either 50 nM VH-Fc 3C9 (yellow) or 50 nM IgG1 m912 (red). The isotype control was labeled in blue. (F) SPR of 3C9 VH and the VH-Fc forms. (G) Lack of non-specific binding measured by a membrane proteome array (MPA). Antibody domain 3C9 was fused to human Fc protein for examination by flow cytometry. VH-Fc 3C9 (20 μg/mL) was tested in a membrane proteome array against 6,000 different human membrane proteins.

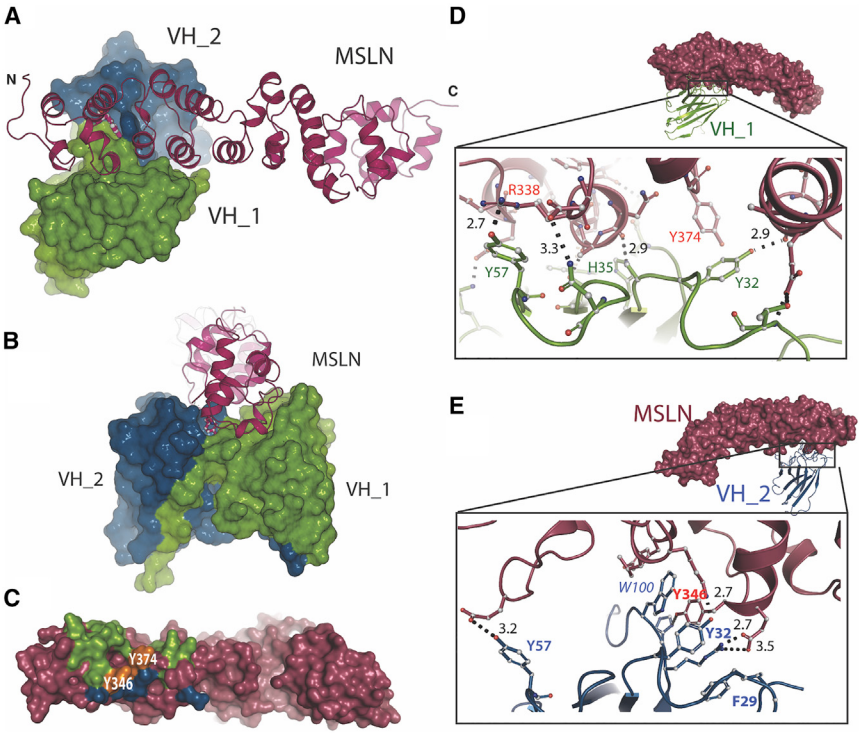

Figure 2. Structure of MSLN-3C9 complex, determined by crystallography

(A) MSLN (coordinate shown from residue 300 to 582, purple) complexed with two VH 3C9 domains, VH_1 and VH_2 (green and blue, respectively). (B) The same structure, viewed from different orientations, highlighting swapping of the C-terminal beta-strands in two VH 3C9 domains. (C) Map of VH_1 (green) and VH_2 (blue) interaction sites on MSLN (purple) with highlight of the locations of Y346 and Y374 (orange). (D) Side chain interaction of MSLN with VH_1 (green) with highlight of Y374 (orange). (E) Side chain interaction of MSLN with VH_2 (blue) with highlight of Y346 (orange). Expanded figures for (A) are shown in Figures S1 and S2; extended figures for (B) and (C) are shown in Figure S3; extended figures for (D) and (E) are shown in Figure S4.

The N-terminal region of MSLN interacts with two VH 3C9 molecules, VH_1 and VH_2, burying a surface area of 799 Å^2 and 391 Å^2, respectively. MSLN interaction with the VH_1 domain involves hairpin loops 1–4 that contact CDR1 (residues 26–33), CDR2 (residues 51–57), and CDR3 loops, and residues from strands 3–5 (of the core beta-sheet) that are contiguous to the CDR2 and CDR3 loops (Figures 2D and S4A–S4E; Table S1). Interactions with the VH_2 domain involve contacts between hairpin loops 2–4 and the CDR3 domain, where W100 is buried in a small hydrophobic pocket formed by residues Y346, L349, Y374, and L377; and involves Y32 (CDR1 loop), which forms a salt bridge with K378 (Figures 2E and S4F–S4H; Table S1). The MSLN-3C9 interaction was validated by mutagenesis experiments; MSLN Y346A and Y374A mutants were tested since they have multiple interactions with both VH_1 and VH_2 (Figure 2C). The Y346A mutant and the double mutant Y346A and Y374A abolished 3C9 binding, while the Y374A mutant had a partial effect (Figure S5).

Overlay between the MSLN-3C9 (this work) and MSLN-MORAb-009 Fab complex shows that MORAb-009 binds the N-terminal region of MSLN more extensively, compared with VH 3C9.[16] For example, although F317 in MSLN deeply interacts with a hydrophobic pocket in MORAb-009, it does not interact with VH 3C9.[16] Although both VH 3C9 and MORAb-009 recognize Y346, MSLN interactions involve largely non-overlapping regions, which is seen when examining the overlaid structures from different orientations (Figures 3A and 3B). Indeed, competitive ELISA assays show no MSLN binding competition between VH 3C9 and MORAb-009 (Figure 3C).

Pharmacokinetics and tumor delivery of VH-Fc 3C9

Tissue distribution and persistence time are important considerations in evaluating the therapeutic potential of an antibody. To investigate these properties, the *in vivo* pharmacokinetics of human IgG1 Fc fused 3C9 was evaluated in a BALB/c nude mouse subcutaneous xenograft cancer model using AsPC-1-luciferase cells. As a control antibody we selected m912, a human monoclonal antibody targeting MSLN that is in Phase II studies.[20] VH-Fc 3C9 and IgG1 m912 labeled with the far infrared dye YF750 SE (named as Ab-YF750) was injected intraperitoneally (i.p.) into tumor-bearing mice, and tumor infiltration was imaged over the course of 10 days (Figure 4A).[22] VH-Fc 3C9 infrared signal was detected as early as 8 h post injection and persisted in tumors for more than 10 days (Figures 4B and 4C). To confirm 3C9 enrichment, tumors were dissected at 3 and 14 days post antibody infusion (experiment endpoint) and assayed for fluorescence. As shown in Figure 4B, the dissected tumor showed fluorescence signal of antibody enrichment in the tumor site. The PBS control did not show any dye enrichment at the tumor site.

VH-Fc 3C9 domain drug conjugate efficaciously inhibits MSLN-positive tumor growth in a mouse xenograft model

To generate and test 3C9 as an ADC, we expressed the VH-Fc format antibody protein, conjugated with monomethyl auristatin E (MMAE), and created VH-Fc 3C9-MMAE antibody ADC. Since MSLN is widely expressed in multiple tumor cell lines, we selected six stable cell lines including A431 (MSLN-negative cells as control) for *in vitro* evaluation of cytotoxicity following treatment with VH-Fc 3C9-MMAE. The efficacy of the ADC in killing tumor cells and non-MSLN cells *in vitro* was monitored by *in vitro* cell viability assay (Figure 5). The VH-Fc 3C9-MMAE ADC exhibited strong killing activity against NCI-H2452 cells, with an estimated EC50 of approximately 8 nM. Additionally, it demonstrated moderate killing activity toward AsPC-1 cells, with an estimated EC50 of 68 nM. However,

Table 1. Data collection, phasing, and refinement statistics

	SSRL (12-1)
Data collection	
Space group	$P4_322$
Cell dimensions	
a, *b*, *c* (Å)	114.1 114.1 340.7
α, β, γ (°)	90, 90, 90
Resolution (Å)	60–2.9
R_{sym} or R_{merge}	0.008(0.45)
$I/\sigma I$ – CC1/2	27.5(1.1) – 99(35)
Completeness (%)	100(100)
Redundancy	25(18)
Phasing	
Wavelength (Se peak)	0.9794
No of sites	8
FOM (SAD)	0.27
Refinement	
Resolution (Å)	37–2.9
No. reflections	51008
R_{work}/R_{free}	22.1/24.4
B-factors	
Protein	65.5
Ligand/ion	N/A
Water	74
R.m.s. deviations	
Bond lengths (Å)	0.009
Bond angles (°)	1.33

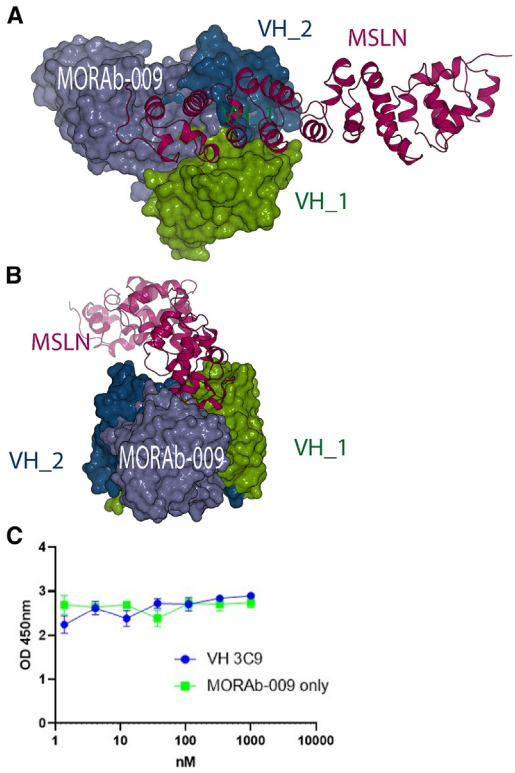

Figure 3. 3C9 does not compete with MORAb-009

(A and B) Surface presentation of MORab-009 (ice blue, PDB 7UED),[16] 3C9 VH_1 (green), and VH_2 (blue) on MSLN (purple, ribbon) are shown from two different orientations. (C) VH 3C9 and MORAb-009 have no competition in competing ELISA.

minimal or no killing effect was observed in PANC-1, SK-OV-3, A431, or A673 cells. These results suggest that the VH-Fc 3C9-MMAE ADC may be particularly effective against cancer cells that exhibit high expression of MSLN.

We evaluated the *in vivo* antitumor activity of VH-Fc 3C9-MMAE ADC in an AsPC-1-Luc cell xenografted model of pancreatic cancer (Figure 6A). Note, the drug conjugating sites in VH-Fc 3C9-MMAE are reduced thiols at the heavy chains, and the average drug antibody ratio (DAR) in our preparation was 3.6, as measured by a contract research organization company. This model of AsPC-1-Luc cell engraftment into BALB/c nude mice (3 million cells per mouse) exhibited an aggressive morbidity phenotype, resulting in animal death within 2–3 weeks and enabling rapid evaluation of whether VH-Fc 3C9 MMAE had a therapeutic impact. Using this model, VH-Fc 3C9 MMAE was found to produce a dose-dependent inhibition of tumor growth. At the highest dose used, 10 mg/kg ADC, significant ($p < 0.0001$) inhibition of tumor growth was observed (Figure 6B); however, the highest dose also caused significant loss of body weight, likely due to the high DAR (~3.6), prompting termination of data collection for this group (Figure 6D). Treatment with 2 mg/kg VH-Fc 3C9 MMAE resulted in significant inhibition of tumor growth (Figures 6B and 6C) and a 33% survival rate in AsPC-1-Luc tumors, compared with 0% in the control group (Figure 6E). We are currently devising strategies to optimize the conjugation process to enhance the performance of the 3C9 antibody domain. These strategies are informed by insights from our structural studies and will be presented in a separate publication.

VH-Fc 3C9 MMAE induces G2/M phase cell-cycle arrest and apoptosis in MSLN-positive tumor cells

As previously documented, MMAE, functioning as a microtubule depolymerization inhibitor, exerts its mechanism of action through tubulin binding, resulting in the inhibition of microtubule polymerization. This interference subsequently disrupts the cellular mitotic process, culminating in cell-cycle arrest and the initiation of apoptosis.[23–25] To evaluate the influence of VH-Fc 3C9 MMAE on the cell cycle of MSLN-positive cells, we conducted a flow cytometry–based cell-cycle analysis involving both AsPC-1 and NCI-H2452 cells. The experimental setup encompassed PBS control, unconjugated VH-Fc 3C9 (1000 nM), and VH-Fc 3C9 MMAE at various concentrations (ranging from 300 nM to 1,000 nM), as illustrated in Figures 7A and 7B. In the presence

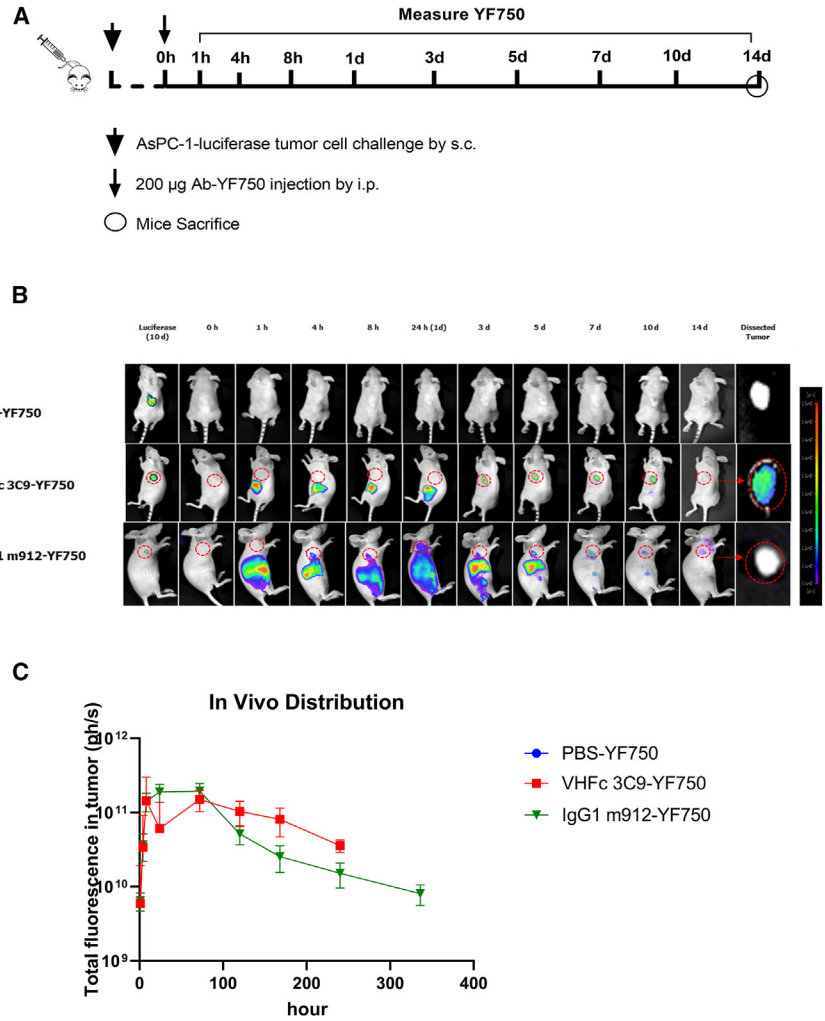

Figure 4. Pharmacokinetics of VH-Fc 3C9-YF750 following i.p. administration and imaging at the indicated time points

(A) Schematic view of the mice injection and data collection. (B) PBS-YF750 group, VH-Fc 3C9-YF750 group, and IgG1 m912-YF750 group; nude mice (n = 5) were administrated VH-Fc 3C9-YF750 or PBS-YF750 by the i.p. route. The fluorescence intensity at the tumor location (red dashed line circle) of mice shown in (B) was measured at the indicated time points. To confirm and pinpoint the location of the tumor cells, the substrate was injected i.p. at 10 d to measure the signal of luciferase from AsPC-1-luciferase cells. To confirm the antibody enriched in the tumor, the tumor was dissected at 14 dpi for YF750 measurement. (C) Total fluorescence in tumor (ph/s). Data are represented as mean ± SEM.

of VH-Fc 3C9 MMAE, concomitant with an escalating concentration of VH-Fc 3C9 MMAE, there was a marked augmentation in the G2/M phase population in both AsPC-1 and NCI-H2452 cells (p values <0.001 in t test comparisons between antibody group and ADC group at 1,000 nM in both cell lines). This effect was coupled with a reduction in the G1 and S phase populations in comparison with the control group. This compelling evidence substantiates the role of VH-Fc 3C9 MMAE in impeding cell-cycle progression within the G2/M phase. To establish whether VH-Fc 3C9 MMAE induces apoptosis in MSLN-positive cells, we evaluated apoptosis levels in AsPC-1 and NCI-H2452 cells subsequent to VH-Fc 3C9 MMAE treatment at different concentrations. This assessment was conducted by quantifying caspase-3/7 activity using a caspase activity assay designed for apoptosis detection. As demonstrated in Figure 7C, the results incontrovertibly confirm the induction of apoptosis by VH-Fc 3C9 MMAE in both AsPC-1 and NCI-H2452 cells. Notably, the threshold concentration of VH-Fc 3C9 MMAE required to initiate caspase-3/7 activity differs notably between the two distinct cell lines.

DISCUSSION

Mesothelin is a validated target for multiple cancers owing to its high expression on cancer cells and low expression in normal tissue. MSLN antibody-based therapeutics have shown efficacy in early clinical trials, primarily targeting solid tumors. Amatuximab, a chimeric monoclonal antibody with potent antibody-dependent cellular cytotoxicity (ADCC) activity, demonstrated moderate antitumor activity in Phase II trials (NCT02357147).[26] In 2020, the FDA approved nivolumab with ipilimumab as first-line treatment for adult patients with unresectable malignant pleural mesothelioma (MPM),[27] offering the possibilities for combination therapies with second-line options. Anetumab ravtansine in combination with targeted agents and chemotherapy showed strong activity in MSLN-expressing human ovarian cancer models.[28] Combination therapy with immune checkpoint blockade anti-PD1 has shown promising antitumor activity of MSLN-specific CAR T cell therapy using fully human scFv m912 in malignant pleural mesothelioma (MPM) (NCT02414269).[29–31] Furthermore, a panel of IgG1 ADCs has shown manageable safety and encouraging preliminary antitumor activity in MSLN-positive solid tumors (NCT01439152, NCT01469793, and NCT02341625). Although CAR-T therapy has limited efficacy against solid tumors, the numerous therapeutics under development suggest that MSLN is a promising druggable target with room for improvement.

Antibodies with satisfactory specificity, high affinity, and *in vivo* persistence are critical to successful therapeutic development. Specificity of mAbs is one key issue that impacts the efficacy of antibody drugs because non-specific interactions can lead to off-target binding, which results in toxicity or fast antibody clearance *in vivo*.[32] 3C9 reported here did not bind the 6,000 human membrane-associated proteins in the MPA assay, indicating low potential for off-target

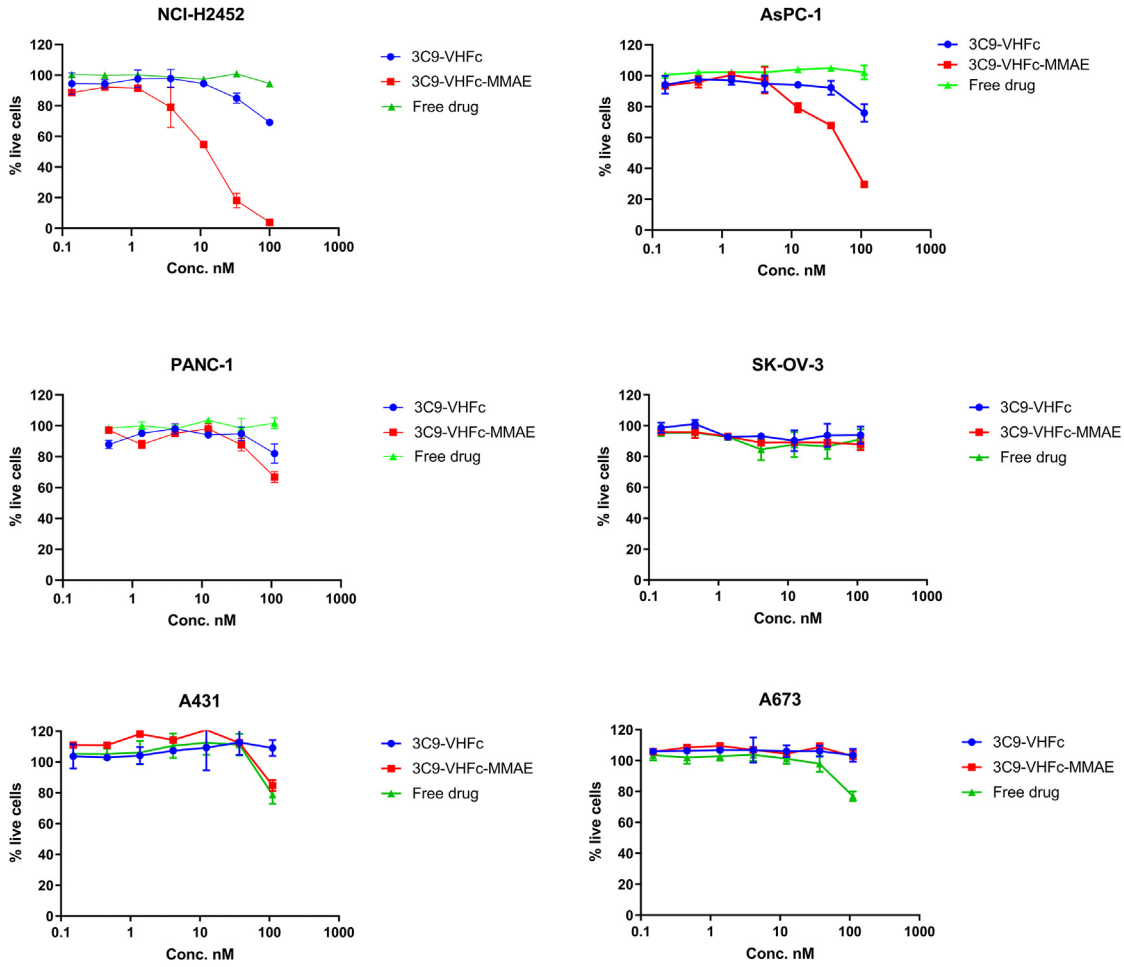

Figure 5. *In vitro* cell viability assays

MSLN-specific antibody-drug conjugates (ADCs) were evaluated using *in vitro* cell viability assays on various human cell lines expressing MSLN, including pancreas adenocarcinoma (AsPC-1), mesothelioma (NCI-H2452), epithelioid carcinomas (PANC-1), and ovarian adenocarcinomas (SK-OV-3). Negative control cell lines, namely epidermoid carcinoma (A-431) and Ewing's sarcoma (A-673), were used for comparison. EC50 values were determined for the cytotoxicity against AsPC-1 and NCI-H2452 cells.

toxicity. Although a potential limitation of human antibody VH domains is insufficient binding affinity for therapeutic application, both VH and VH-Fc 3C9 showed less than a 10-nM dissociation constant against MSLN. Based on the structural study, the binding involves hydrophobic interaction at Y346 and Y374, explaining the high binding affinity of VH 3C9. The VH 3C9 also has the advantage of being fully human and aggregation resistant, allowing for potential re-dosing or multiple therapeutic avenues due to a lower immunogenicity profile. In addition, VH-Fc 3C9 accumulated at *in vivo* tumor sites as early as 8 h after intraperitoneal administration and persisted in tumors for more than 10 days.

In theory, the smaller size of antibody domains would allow for better tissue penetration. There are indeed some examples that suggest antibody domains may have better penetration and persistence in solid tumors.[22,33] However, in our assay, we did not observe an improvement in tissue penetration of the VH-Fc 3C9 compared with the full-length IgG1 m912. One possible reason is that the IgG1 m912 may be enriched in the stroma region, which could result in better signal but lower uptake by the tumor cells. To address this, a more sensitive approach is needed to detect the penetration and antibody uptake by the tumor cells.[34,35] Domain drug conjugates to cytotoxic payloads (DCC) have been evaluated recently in different tumor models and could be a good way to overcome penetration and recruitment issues that CAR-T therapies face.[36,37] VH-Fc 3C9 MMAE inhibited tumor growth at a dose of 2 mg/kg. Toxicity was observed in mice at a dose of 10 mg/kg, suggesting that further optimization of the ADC conjugation approach may be necessary to reduce toxicity. In a recent Phase I/IIa trial of BMS-986148, 13% of patients experienced severe treatment-related adverse events that led to discontinuation of therapy.[38] Similar situations occurred in the Phase I studies of DMOT4039A and anetumab ravtansine (BAY 94–9343),

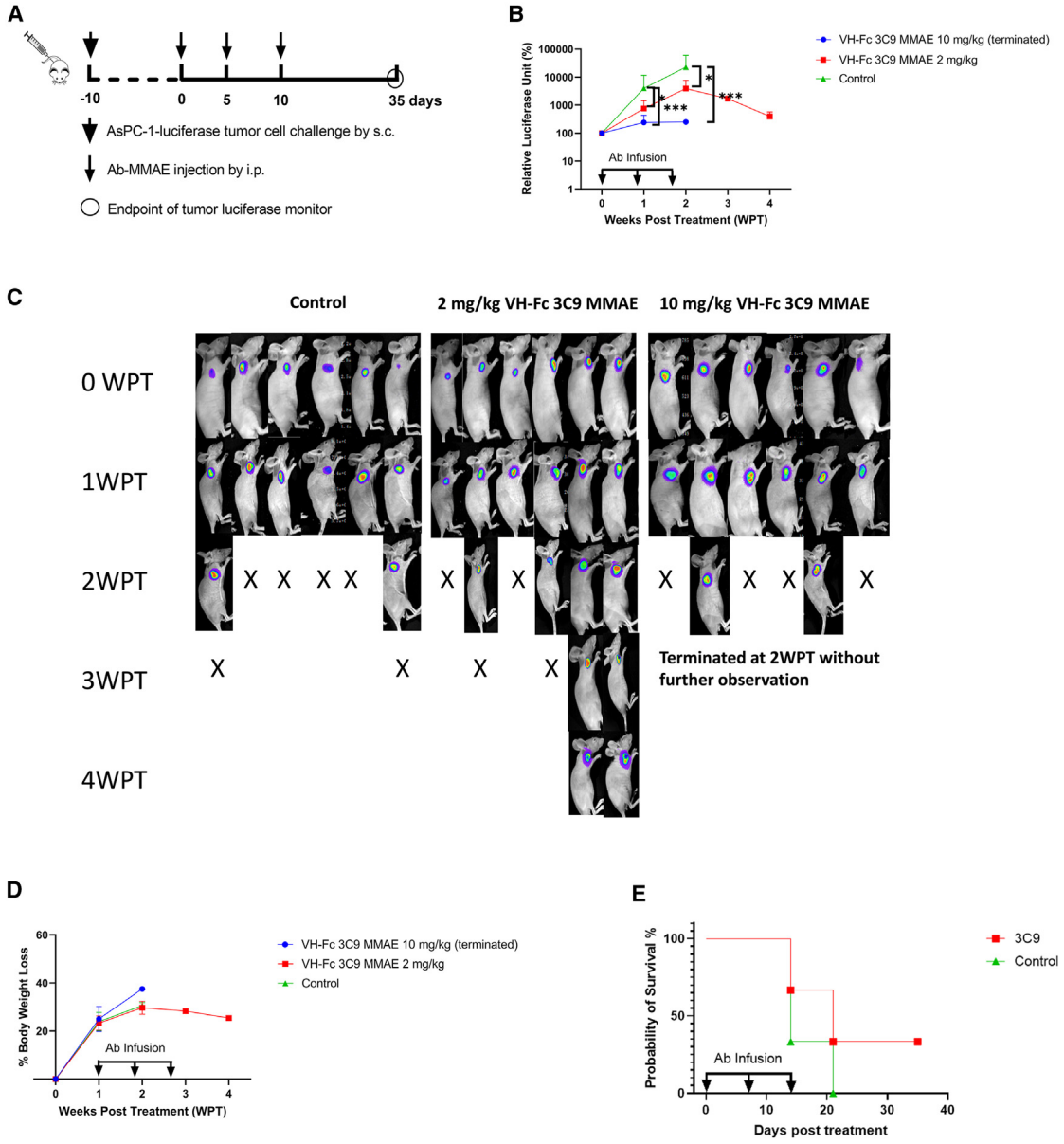

Figure 6. *In vivo* study of VH-Fc 3C9 ADC

(A) Schematic view of the mice injection and data collection. (B) Relative luciferase signals of tumor in control group and ADC groups. $p < 0.01$; ***, $p < 0.001$; ****, $p < 0.0001$. (C) Fluorescence measurements of control group and ADC group. (D) Body weight measurement of control group and ADC groups. (E) Survival rate measurement.

despite their tolerable and manageable safety profiles.[39,40] Developing new safe drugs for ADC conjugation and reducing the DAR to a safe level will be the direction for future ADC development against MSLN-expressing cancers. The present study investigated the impact of VH-Fc 3C9 MMAE on cell-cycle progression and apoptosis induction in MSLN-positive cells, specifically AsPC-1 and NCI-H2452 cells. Our findings provide valuable insights into the mechanistic action of VH-Fc 3C9 MMAE and its potential as an anti-cancer therapeutic agent. Continuous optimization of VH-Fc 3C9 and conjugation with new drugs have promise for the development of new therapies against pancreatic cancer. It is worth noting that 3C9 does not exhibit cross-reactivity to mouse MSLN; however, it does demonstrate cross-reactivity to cynomolgus MSLN. This characteristic will be advantageous for facilitating safety evaluations in cynomolgus macaques (Figure S6).

The crystal structure of MSLN presented here enables a discussion of epitope and antibody binding to MSLN. Given the limited efficacy of the drugs in development, the unique epitope may improve antibody function by utilizing a different mechanism of action, as has been seen

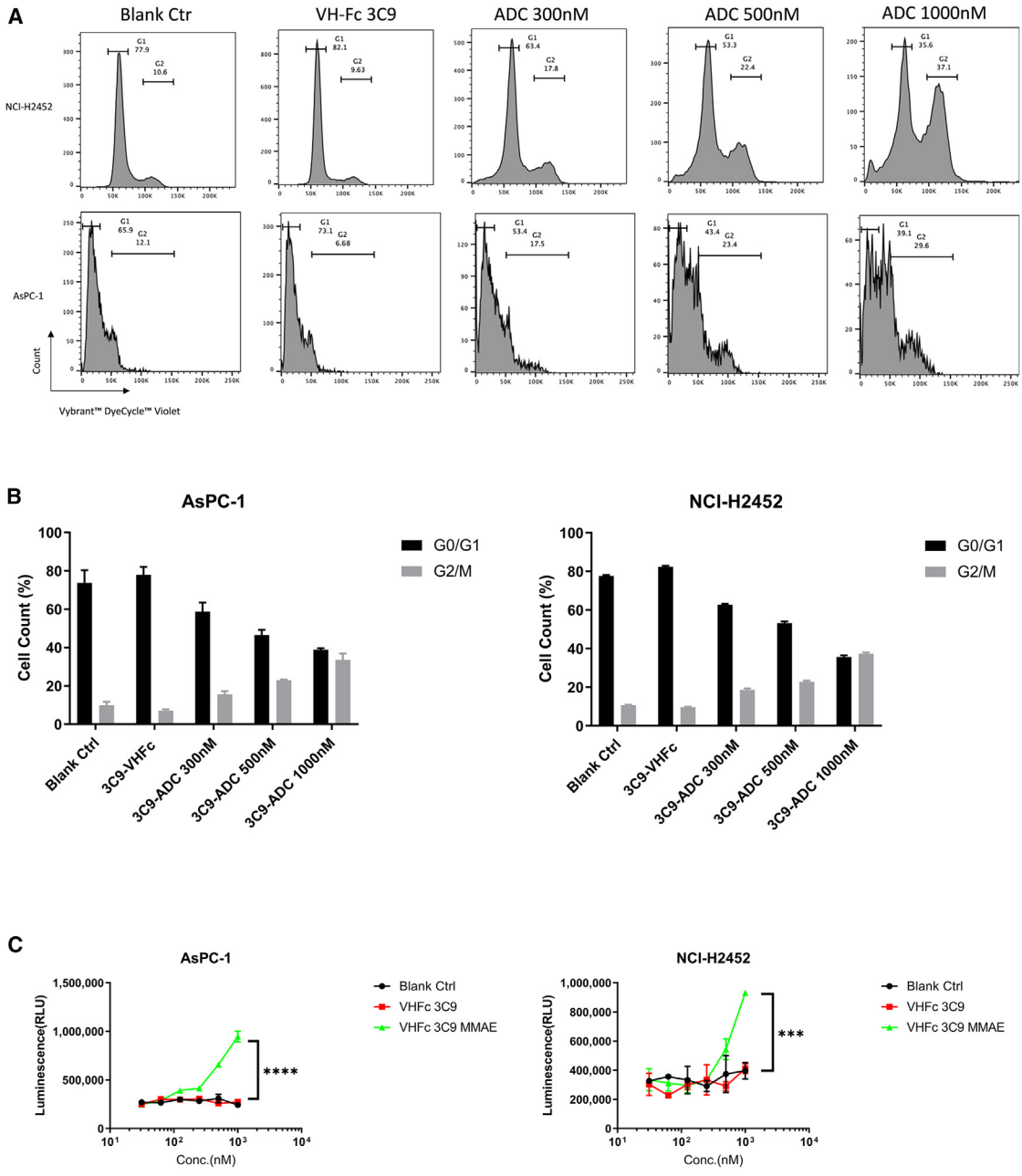

Figure 7. Induction of cell-cycle arrest and apoptosis by VH-Fc 3C9 MMAE in MSLN-positive tumor cells

(A) Flow cytometric analysis of DNA content distribution. The histogram displays live cells stained with Vybrant DyeCycle Violet stain, with clear labeling of G1 and G2 phase histogram peaks. These results are representative of two independent experiments. (B) Quantitative assessment of the G0/G1 and G2/M phases in AsPC-1 cells and NCI-H2452 cells upon treatment, indicating the effects of VH-Fc 3C9 MMAE. (C) Detection of Caspase-3 or -7 activity. Data shown represent results from two independent experiments and are presented as mean values ± standard error of the mean (SEM). Statistical analysis was conducted using a two-way repeated-measures ANOVA test, with significance levels denoted as follows: *p < 0.05; **p < 0.01; ***p < 0.001; ****p < 0.0001.

for other antibody targets such as CD20.[41] We now know that the epitope of 3C9 is quite close to the epitopes of MORAb-009 Fab[16]; however, there is no competition observed between 3C9 and amatuximab. Several biparatopic antibodies have been reported in different tumor models.[42–45] In a breast cancer model, a biparatopic antibody shows enhanced avidity and cross-linking activity to promote HER2 clustering and lysosomal degradation.[43] A biparatopic antibody including VH 3C9 and Fab MORAb-009 may further increase the avidity without a significant increase of antibody size.[46,47] Additionally, MORAb-009 mechanisms have been well studied for ADCC as

well as antibody blocking of MSLN binding to metastatic co-factors such as CA125/MUC16 which could further improve functionality of a biparatopic antibody, especially if 3C9 contributes via different mechanisms.[48] Finally, the structure of MSLN-3C9 provides useful information and guidance to select site-specific mutation sites for drug conjugation without affecting affinity. This information can be utilized to construct more potent and efficient ADCs with controlled DARs and reduced toxicity.

MSLN-targeting CAR-T therapy has shown limited activity in patients, possibly due to various factors such as the clinical antibodies in CARs not targeting membrane-proximal epitope. Recent studies have demonstrated that CAR-T cells targeting membrane-proximal epitopes in MSLN on tumor cells showed increased tumor infiltration and persistence, as well as efficacy.[49,50] Additionally, CAR T cells that target the juxtamembrane region of MSLN have been developed and show high activity. While the principles are not identical, similar effects have been observed in a study of CD22 CAR-T cells targeting the membrane-proximal epitope of CD22.[51] Based on this perspective, 3C9 may not be the best candidate for monoCAR-T development, but it can aid in the design of a biepitopic CAR. A recent study demonstrated that a biepitopic CAR-T targeting B cell maturation antigen (BCMA) achieved a high objective response rate of 88.2% in treating relapsed/refractory multiple myeloma.[52]

In summary, we isolated and characterized a novel antibody VH domain, 3C9, with high affinity to MSLN, aggregation resistance, and high specificity. The 3C9 VH domain exhibited specific tumor cell killing in domain drug conjugate formats. Pharmacokinetic studies and animal trials of ADCs demonstrate the potential of 3C9 as a clinical candidate for further development. Furthermore, the full-length structure of the MSLN-3C9 complex, determined in this study, provides insights into the relative binding sites of the antibody. This information can guide the optimization of the antibody to increase its affinity and reveals suitable amino acids for site-specific conjugation of drugs for construction of more efficient ADCs with controlled DARs.

MATERIALS AND METHODS

Expression and purification of MSLN protein, VH binders, and VH bivalent proteins

The gene of human MSLN was synthesized by IDT (Coralville, Iowa) with the sequence obtained from Uniprot (https://www.uniprot.org/uniprot/Q13421). The MSLN domain (residues 296–606) were cloned into an expression plasmid. This plasmid contains a CMV promotor and woodchuck posttranscriptional regulatory elements with a His tag. Proteins were purified by Ni-NTA (GE Healthcare). MSLN-specific VH domains were in the pComb3x vector and purified from *Escherichia coli* HB2151 bacterial culture at 30°C for 16 h with stimulation by 1 mM IPTG. Cells were lysed by Polymyxin B (Sigma-Aldrich). Lysates were spun down and supernatant was loaded over Ni-NTA (GE Healthcare). For conversion to Fc-fusion, the VH gene was re-amplified and re-cloned into pSectaq vector containing human Fc. VH-Fc proteins were expressed in the Expi293 expression system (Thermo Fisher Scientific) and purified with protein A resin (GenScript). Buffer replacement in protein purification used Column PD 10 desalting column (GE Healthcare). All protein purity was estimated as >95% by SDS-PAGE and protein concentration was measured spectrophotometrically (NanoVue, GE Healthcare). Further details can be found in our previous publication.[53] Cell lines used for *in vitro* cell viability assays were purchased from ATCC (https://www.atcc.org/, USA): NCI-H2452 (Cat# CRL-5946), AsPC-1 (CAT# CRL-1682), PANC-1 (CAT# CRL-1469), 293T (CAT# CRL-3216), A-673 (CAT# CRL-1598), A-431 (CAT# CRL-1555), and SK-OV-3 (CAT# HTB-77).

ELISA and SPR

For ELISA assays, antigen protein, human MSLN, was coated on a 96-well plate (Costar) at 50 ng/well in PBS overnight at 4°C. For the soluble VH binding assay, horseradish peroxidase (HRP)-conjugated mouse anti-FLAG tag antibody (A8592, Sigma-Aldrich) was used to detect VH binding. For detection of human Fc protein, HRP-goat anti-human IgG Fc secondary antibody (A18817, Thermo Fisher Scientific) was used. ELISA assay was also performed using mouse MSLN (Cat: 5A0830-M49H-B) and Cynomolgus MSLN (Cat: 91009-C08H), purchased from Sino Biological US Inc. (Houston, TX, USA) for comparison. For the competition ELISA, 200 nM of IgG1 m912, or 50 nM VH-Fc 3C9 was incubated with serially diluted VH proteins, and the mixtures were added to antigen-coated wells. After washing, competition was detected by HRP-goat anti-human IgG Fc secondary antibody (A18817, Thermo Fisher Scientific). The kinetics of the antibody fragments were determined using a Biacore X100 (GE Healthcare). Human MSLN (purified from Expi 293 cells) in 0.3-μM solution was immobilized onto a CM5 sensor chip (GE Healthcare, BR100012) by amine coupling. The antibody fragments diluted in HBS-EP buffer (10 mM HEPES, 150 mM NaCl, 3 mM EDTA, and 0.005% surfactant P20, pH 7.4) were injected over an immobilized surface (200–400 RU) for 90 s at a rate of 50 μL/min, followed by dissociation for 600 s. After each sample injection, the surface was regenerated by injection of regeneration solution (10 mM Glycine/HCl buffer, with 10% glycerol at pH 2.0 for VH and VH-Fc binders). The kinetic values, ka, kd, and KD were calculated using the BiacoreX100 Evaluation Software (GE Healthcare).

ADC generation

Monomethyl auristatin E (MMAE) was conjugated to VH-Fc 3C9 via the conjugation kit (CM11409 CellMosaic, Inc., MA). Antibody labeling sites: Reduced thiols at heavy chains. Antibody drug linkage: Cathepsin B cleavable VC-PAB linkage. The protein was washed and concentrated using 30 kDa Amicon centrifugal filter unit (Millipore Sigma CAT#UFC8030). ADC was characterized by ELISA, SEC analysis, and non-reducing SDS-PAGE analysis (Figures S7 and S8) before DAR measurement by intact mass LC/MS analysis and animal trials.

Cell viability assays

Cell viability was measured using CellTiter-Glo (G7570, Promega) or LDH-Glo (J2380, Promega). Briefly, MSLN-positive or -negative cells

were plated into 96 wells, allowing attachment and growth for 24 h, then triplicate wells were treated with ADCs, naked antibodies, free drugs, or ADCs plus competitor antibodies. Three to 5 days later, when untreated control wells were 70%–90% confluent, reagent was added to the plates according to the supplier's instructions. Wells treated identically but wells without cells were used to subtract background. Fluorescence (ex: 570 nm, Em: 585 nm) was measured using a CLARIOstar microplate reader (BMG Labtech) and data analyzed using GraphPad Prism 8 software. Percentages were calculated following the commercial protocol stated in the kit. For LDH-based cell viability assay, % Cytotoxicity = 100 × (Experimental LDH Release – Medium Background)/(Maximum LDH Release Control – Medium Background).

Size-exclusion chromatography

SEC was employed to determine the apparent molecular size of VH 3C9 using the Superdex 200 Increase 10/300 GL chromatography column (GE Healthcare, Cat. No. 28990944). In each run, a 150-μL filtered protein solution (1–2 mg/mL) in phosphate-buffered saline (PBS) was injected into the column and eluted at a flow rate of 0.4 mL/min. The elution volume of the injected protein was used to estimate its apparent molecular mass, with protein molecular mass standards of Ferritin (Mr 440,000 kDa), Aldolase (Mr 158,000 kDa), Conalbumin (Mr 75,000 kDa), Ovalbumin (Mr 44,000 kDa), Carbonic anhydrase (Mr 29,000 kDa), and Ribonuclease A (Mr 13,700 kDa) employed for calibration purposes.

Flow cytometry

Aliquots of detached cells with a viability of over 95% were incubated with human Fc block (Miltenyi Biotec, CAT# 130-059-901) in FACS buffer (PBS+3% BSA) on ice for 30 min. Subsequently, the cells were stained with the primary antibody (isotype control, IgG1 m912, or VH-Fc 3C9) at a concentration of 50 nM in FACS buffer for 1 h on ice. After washing away unbound antibodies with medium, cells were incubated with the secondary antibody, goat anti-human IgG conjugated with PE (Sigma), for 30 min on ice. Finally, the cells were washed, resuspended in PBS+0.5% BSA, and subjected to flow cytometry analysis using FACSCalibur (Beckton Dickinson).

Membrane Proteome Array

Integral Molecular, Inc. (Philadelphia, PA) performed specificity testing of VH-Fc 3C9 using the MPA platform. The MPA comprises 6,000 different human membrane protein clones, each overexpressed in live cells from expression plasmids that are individually transfected in separate wells of a 384-well plate. The entire library of plasmids is arrayed in duplicate in a matrix format and transfected into engineered HEK293T cells, followed by incubation for 36 h to allow protein expression. Before specificity testing, optimal antibody concentrations for screening were determined by using cells expressing positive (membrane-tethered protein A) and negative (mock-transfected) binding controls, followed by flow cytometric detection with an Alexa Fluor-conjugated secondary antibody (Jackson ImmunoResearch Laboratories) to confirm cell-specific binding. Based on the assay setup results, the VH-Fc protein (20 μg/mL) was added to the MPA, and binding across the protein library was measured on an iQue3 (Ann Arbor, MI) using the same fluorescently labeled secondary antibody. To ensure data validity, each array plate contained positive (Fc-binding; MSLN protein) and negative (empty vector) controls. Targets identified in the assay were confirmed in a second flow cytometric experiment by using serial dilutions of the test antibody, and the identity of each target was also confirmed by sequencing.

Crystallization, data collection, and refinement

MSLN complex with VH 3C9 was prepared by injecting the protein mixture to Superdex 75 column (GE Healthcare, Chicago, IL), and concentrated to 12 mg/mL. To allow multi-wavelength anomalous diffraction analysis, selenomethionine (Se-Met) labeled VH 3C9 was also prepared by expressing the protein in *E. coli* BL21(DE3) cells, using a minimum media with Se-Met and supplemental amino acids to reduce Se-Met toxicity (L-isoleucine, L-leucine, L-lysine, L-phenylalanine, L-threonine, and L-valine) prior to the induction.[54] The Se-Met incorporation to VH 3C9 was confirmed by mass spectrometry, 15122.52 Da (theoretical mass, 15123.23 Da), by comparing the mass without Se-Met labeling, 15028.68 Da (theoretical mass 15029.41 Da), using an LC-TOF mass spectrometry (Bruker Daltonics, Billerica, MA). Data were collected at the 12-2 SSRL (wavelength 0.9795 Å). Diffraction data were processed, integrated, and scaled using XDS. The structure was solved by single-wavelength diffraction analysis. Model building and refinement were performed using Coot and Phenix[55,56] (Table 1). The coordinates are available in the Protein DataBank (ID: 8FSL).

Animal model generation

Animal trials were completed in Abrev Inc (both *in vivo* ADC efficacy and distribution).[22] Briefly, BALB/c nude mice (18–22 g, female, Qls03-0102) were purchased from Qing Long Shan Animal Center (Nanjing, China). The nude mice were kept following Laboratory Animal center's standard operational procedures. Four- to 6-week old nude mice were injected subcutaneously with 5.0×10^5 AsPC-1-luciferase cells. Seven days later, the tumor size was about 200 mm^3 and was visible. Antibodies were then injected i.p., as described in the context.

Spatial distribution of VH-Fc 3C9 *in vivo*

Antibodies VH-Fc 3C9 and IgG1 m912 were labeled with far infrared dye YF750 SE (US EVERBRIGHT INC, YS0056) (named as Nbs-YF750). ELISA confirmed that conjugation does not affect the EC50 values of both VH-Fc 3C9 and IgG1 m912 against MSLN. A PBS control was also treated similarly with dye. Five mice (M01-05) were injected i.p. with 200 μg (∼10 mg/kg, mice) purified Abs-YF750. Tumor fluorescence was thus measured accordingly. Images were observed at Ex: 740 nm/Em: 780 nm by NightOWL LB 983 (Berthold, Germany) at the indicated time point. To confirm the antibody enriched in the tumor, the tumor was dissected at 3 days post antibody infusion (dpi) and 14 dpi (endpoint), respectively. To pinpoint the location of the tumor cells, luciferase substrate was injected via i.p. to measure the signal

of luciferase from AsPC-1-luciferase cells. Images were analyzed using Indigo imaging software Ver. A 01.19.01.

Cell-cycle arrest and apoptosis assay

The cell-cycle analysis assay was performed using Vybrant DyeCycle Violet stain (V35003, Invitrogen, USA) following established protocols. Specifically, $3*10^5$ AsPC-1 cells per well were seeded into a 6-well plate and allowed to incubate for 24 h. Subsequently, cells were treated with ADC or VH-Fc for 72 h prior to analysis. For NCI-H2452 cells, the incubation period was 48 h before analysis. Flow cytometry was then utilized for cell analysis, adhering to established procedures. The cells were subjected to various drug regimens, including a blank control of PBS, a negative control of 1,000 nM VH-Fc 3C9, and experimental controls of VH-Fc 3C9 MMAE at doses of 300 nM, 500 nM, and 1,000 nM, respectively. In the caspase activity assay used for apoptosis detection, the Caspase-Glo 3/7 Assay System (G8091, Promega, USA) was employed, following standardized protocols. To prepare for this assay, 5000 AsPC-1 cells per well were seeded into a 96-well plate and allowed to incubate for 24 h. Subsequently, cells were treated with serially diluted ADC or VH-Fc for 96 h. NCI-H2452 cells, on the other hand, were treated for 72 h before measurement. Apoptosis levels were quantified by measuring luminescent signals.

Statistical analysis *in vivo* study

Significance was tested using two-way repeated-measures ANOVA with Bonferroni's post hoc test: ****$p < 0.0001$; ***$p < 0.001$; **$p < 0.01$; *$p < 0.05$ between the indicated groups.

DATA AND CODE AVAILABILITY

Protein coordinate is available (PDB: 8FSL).

SUPPLEMENTAL INFORMATION

Supplemental information can be found online at https://doi.org/10.1016/j.omto.2023.09.002.

ACKNOWLEDGMENTS

We would like to thank the members of the Center for Antibody Therapeutics at the University of Pittsburgh for their helpful discussions. We thank Andrew Hinck for the use of the Biacore X100 instrument and Teresa Brosenitsch for reading the manuscript. This work was supported by the University of Pittsburgh Medical Center.

AUTHOR CONTRIBUTIONS

Z.S. and D.S.D. designed and supervised the project. Z.S. identified and characterized antibodies, ADCs, and *in vivo* assays. X.C. produced recombinant MSLN proteins and antibodies for crystallization studies, conducted tests for ADC conjugation as well as *in vitro* cytotoxicity assessments, and executed assays to evaluate cell-cycle arrest and induction of apoptosis. C.A. performed UPLC for DAR determination and cell cytotoxicity assays. C.C. produced the VH-Fc protein for assay. D.J. and W.L. studied the modeling of epitope of antibody. M.G., G.L, R.I., and G.C. did crystallization and production of selenomethionyl labeled proteins. T.I., M.G., and R.I. conducted SPR experiments and SEC experiments to verify the binding site. G.C. determined crystal structure. Z.S. wrote the first draft of the article. C.A. and X.C. revised the draft. Z.S., J.W.M., and D.S.D. discussed the results and further revised the manuscript. All authors contributed to the final manuscript.

DECLARATION OF INTERESTS

Z.S., J.W.M., and D.S.D. are co-inventors of a patent filed by the University of Pittsburgh, related to 3C9 described in this paper.

REFERENCES

1. Liu, W., Tai, C.H., Liu, X., and Pastan, I. (2022). Anti-mesothelin immunotoxin induces mesothelioma eradication, anti-tumor immunity, and the development of tertiary lymphoid structures. Proc. Natl. Acad. Sci. USA *119*, e2214928119. https://doi.org/10.1073/pnas.2214928119.

2. Hassan, R., and Ho, M. (2008). Mesothelin targeted cancer immunotherapy. Eur. J. Cancer *44*, 46–53. https://doi.org/10.1016/j.ejca.2007.08.028.

3. Hassan, R., Remaley, A.T., Sampson, M.L., Zhang, J., Cox, D.D., Pingpank, J., Alexander, R., Willingham, M., Pastan, I., and Onda, M. (2006). Detection and quantitation of serum mesothelin, a tumor marker for patients with mesothelioma and ovarian cancer. Clin. Cancer Res. *12*, 447–453. https://doi.org/10.1158/1078-0432.CCR-05-1477.

4. Hassan, R., Thomas, A., Alewine, C., Le, D.T., Jaffee, E.M., and Pastan, I. (2016). Mesothelin Immunotherapy for Cancer: Ready for Prime Time? J. Clin. Oncol. *34*, 4171–4179. https://doi.org/10.1200/JCO.2016.68.3672.

5. Klampatsa, A., Dimou, V., and Albelda, S.M. (2021). Mesothelin-targeted CAR-T cell therapy for solid tumors. Expert Opin. Biol. Ther. *21*, 473–486. https://doi.org/10.1080/14712598.2021.1843628.

6. Adusumilli, P.S., Cherkassky, L., Villena-Vargas, J., Colovos, C., Servais, E., Plotkin, J., Jones, D.R., and Sadelain, M. (2014). Regional delivery of mesothelin-targeted CAR T cell therapy generates potent and long-lasting CD4-dependent tumor immunity. Sci. Transl. Med. *6*, 261ra151. https://doi.org/10.1126/scitranslmed.3010162.

7. Adusumilli, P.S., Zauderer, M.G., Rivière, I., Solomon, S.B., Rusch, V.W., O'Cearbhaill, R.E., Zhu, A., Cheema, W., Chintala, N.K., Halton, E., et al. (2021). A Phase I Trial of Regional Mesothelin-Targeted CAR T-cell Therapy in Patients with Malignant Pleural Disease, in Combination with the Anti-PD-1 Agent Pembrolizumab. Cancer Discov. *11*, 2748–2763. https://doi.org/10.1158/2159-8290.CD-21-0407.

8. Ma, J., Tang, W.K., Esser, L., Pastan, I., and Xia, D. (2012). Recognition of mesothelin by the therapeutic antibody MORAb-009: structural and mechanistic insights. J. Biol. Chem. *287*, 33123–33131. https://doi.org/10.1074/jbc.M112.381756.

9. Sun, Z., Li, W., Mellors, J.W., Orentas, R., and Dimitrov, D.S. (2022). Construction of a Large Size Human Immunoglobulin Heavy Chain Variable (VH) Domain Library, Isolation and Characterization of Novel Human Antibody VH Domains Targeting PD-L1 and CD22. Front. Immunol. *13*, 869825. https://doi.org/10.3389/fimmu.2022.869825.

10. Li, C., Zhan, W., Yang, Z., Tu, C., Hu, G., Zhang, X., Song, W., Du, S., Zhu, Y., Huang, K., et al. (2022). Broad neutralization of SARS-CoV-2 variants by an inhalable bispecific single-domain antibody. Cell *185*, 1389–1401.e18. https://doi.org/10.1016/j.cell.2022.03.009.

11. Danis, C., Dupré, E., Zejneli, O., Caillierez, R., Arrial, A., Bégard, S., Mortelecque, J., Eddarkaoui, S., Loyens, A., Cantrelle, F.X., et al. (2022). Inhibition of Tau seeding by targeting Tau nucleation core within neurons with a single domain antibody fragment. Mol. Ther. *30*, 1484–1499. https://doi.org/10.1016/j.ymthe.2022.01.009.

12. Sun, Z., Chen, C., Li, W., Martinez, D.R., Drelich, A., Baek, D.S., Liu, X., Mellors, J.W., Tseng, C.T., Baric, R.S., and Dimitrov, D.S. (2020). Potent neutralization of SARS-CoV-2 by human antibody heavy-chain variable domains isolated from a large library with a new stable scaffold. MAbs *12*, 1778435. https://doi.org/10.1080/19420862.2020.1778435.

13. Cordy, J.C., Morley, P.J., Wright, T.J., Birchler, M.A., Lewis, A.P., Emmins, R., Chen, Y.Z., Powley, W.M., Bareille, P.J., Wilson, R., et al. (2015). Specificity of human

anti-variable heavy (VH) chain autoantibodies and impact on the design and clinical testing of a VH domain antibody antagonist of tumour necrosis factor-alpha receptor 1. Clin. Exp. Immunol. *182*, 139–148. https://doi.org/10.1111/cei.12680.

14. Han, L., Zhang, J.S., Zhou, J., Zhou, K.S., Xu, B.L., Li, L.L., Fang, B.J., Yin, Q.S., Zhu, X.H., Zhou, H., et al. (2021). Single VHH-directed BCMA CAR-T cells cause remission of relapsed/refractory multiple myeloma. Leukemia *35*, 3002–3006. https://doi.org/10.1038/s41375-021-01269-3.

15. Arbabi-Ghahroudi, M. (2022). Camelid Single-Domain Antibodies: Promises and Challenges as Lifesaving Treatments. Int. J. Mol. Sci. *23*, 5009. https://doi.org/10.3390/ijms23095009.

16. Zhan, J., Lin, D., Watson, N., Esser, L., Tang, W.K., Zhang, A., Liu, X., Hassan, R., Gleinich, A., Shajahan, A., et al. (2023). Structures of Cancer Antigen Mesothelin and Its Complexes with Therapeutic Antibodies. Cancer Res. Commun. *3*, 175–191. https://doi.org/10.1158/2767-9764.CRC-22-0306.

17. Hassan, R., Cohen, S.J., Phillips, M., Pastan, I., Sharon, E., Kelly, R.J., Schweizer, C., Weil, S., and Laheru, D. (2010). Phase I clinical trial of the chimeric anti-mesothelin monoclonal antibody MORAb-009 in patients with mesothelin-expressing cancers. Clin. Cancer Res. *16*, 6132–6138. https://doi.org/10.1158/1078-0432.CCR-10-2275.

18. Lee, J.H., Kim, H., Yao, Z., Lee, S.J., Szajek, L.P., Grasso, L., Pastan, I., and Paik, C.H. (2015). Tumor and organ uptake of (64)Cu-labeled MORAb-009 (amatuximab), an anti-mesothelin antibody, by PET imaging and biodistribution studies. Nucl. Med. Biol. *42*, 880–886. https://doi.org/10.1016/j.nucmedbio.2015.07.008.

19. Kim, H., Gao, W., and Ho, M. (2013). Novel immunocytokine IL12-SS1 (Fv) inhibits mesothelioma tumor growth in nude mice. PLoS One *8*, e81919. https://doi.org/10.1371/journal.pone.0081919.

20. Feng, Y., Xiao, X., Zhu, Z., Streaker, E., Ho, M., Pastan, I., and Dimitrov, D.S. (2009). A novel human monoclonal antibody that binds with high affinity to mesothelin-expressing cells and kills them by antibody-dependent cell-mediated cytotoxicity. Mol. Cancer Ther. *8*, 1113–1118. https://doi.org/10.1158/1535-7163.MCT-08-0945.

21. Li, W., Schäfer, A., Kulkarni, S.S., Liu, X., Martinez, D.R., Chen, C., Sun, Z., Leist, S.R., Drelich, A., Zhang, L., et al. (2020). High Potency of a Bivalent Human VH Domain in SARS-CoV-2 Animal Models. Cell *183*, 429–441.e16. https://doi.org/10.1016/j.cell.2020.09.007.

22. Wu, X., Cheng, L., Fu, M., Huang, B., Zhu, L., Xu, S., Shi, H., Zhang, D., Yuan, H., Nawaz, W., et al. (2021). A potent bispecific nanobody protects hACE2 mice against SARS-CoV-2 infection via intranasal administration. Cell Rep. *37*, 109869. https://doi.org/10.1016/j.celrep.2021.109869.

23. Tsujii, S., Serada, S., Fujimoto, M., Uemura, S., Namikawa, T., Nomura, T., Murakami, I., Hanazaki, K., and Naka, T. (2021). Glypican-1 Is a Novel Target for Stroma and Tumor Cell Dual-Targeting Antibody-Drug Conjugates in Pancreatic Cancer. Mol. Cancer Ther. *20*, 2495–2505. https://doi.org/10.1158/1535-7163.MCT-21-0335.

24. Panchamoorthy, G., Jin, C., Raina, D., Bharti, A., Yamamoto, M., Adeebge, D., Zhao, Q., Bronson, R., Jiang, S., Li, L., et al. (2018). Targeting the human MUC1-C oncoprotein with an antibody-drug conjugate. JCI Insight *3*, e99880. https://doi.org/10.1172/jci.insight.99880.

25. Zheng, C., Zhou, D., Li, W., Duan, Y., Xu, M., Liu, J., Cheng, J., Xiao, Y., Xiao, H., Gan, T., et al. (2023). Therapeutic efficacy of a MMAE-based anti-DR5 drug conjugate Oba01 in preclinical models of pancreatic cancer. Cell Death Dis. *14*, 295. https://doi.org/10.1038/s41419-023-05820-1.

26. Hassan, R., Kindler, H.L., Jahan, T., Bazhenova, L., Reck, M., Thomas, A., Pastan, I., Parno, J., O'Shannessy, D.J., Fatato, P., et al. (2014). Phase II clinical trial of amatuximab, a chimeric antimesothelin antibody with pemetrexed and cisplatin in advanced unresectable pleural mesothelioma. Clin. Cancer Res. *20*, 5927–5936. https://doi.org/10.1158/1078-0432.CCR-14-0804.

27. Baas, P., Scherpereel, A., Nowak, A.K., Fujimoto, N., Peters, S., Tsao, A.S., Mansfield, A.S., Popat, S., Jahan, T., Antonia, S., et al. (2021). First-line nivolumab plus ipilimumab in unresectable malignant pleural mesothelioma (CheckMate 743): a multicentre, randomised, open-label, phase 3 trial. Lancet *397*, 375–386. https://doi.org/10.1016/S0140-6736(20)32714-8.

28. Quanz, M., Hagemann, U.B., Zitzmann-Kolbe, S., Stelte-Ludwig, B., Golfier, S., Elbi, C., Mumberg, D., Ziegelbauer, K., and Schatz, C.A. (2018). Anetumab ravtansine inhibits tumor growth and shows additive effect in combination with targeted agents and chemotherapy in mesothelin-expressing human ovarian cancer models. Oncotarget *9*, 34103–34121. https://doi.org/10.18632/oncotarget.26135.

29. Cadilha, B.L., Benmebarek, M.R., Dorman, K., Oner, A., Lorenzini, T., Obeck, H., Vänttinen, M., Di Pilato, M., Pruessmann, J.N., Stoiber, S., et al. (2021). Combined tumor-directed recruitment and protection from immune suppression enable CAR T cell efficacy in solid tumors. Sci. Adv. *7*, eabi5781. https://doi.org/10.1126/sciadv.abi5781.

30. Xie, Y.J., Dougan, M., Jailkhani, N., Ingram, J., Fang, T., Kummer, L., Momin, N., Pishesha, N., Rickelt, S., Hynes, R.O., and Ploegh, H. (2019). Nanobody-based CAR T cells that target the tumor microenvironment inhibit the growth of solid tumors in immunocompetent mice. Proc. Natl. Acad. Sci. USA *116*, 7624–7631. https://doi.org/10.1073/pnas.1817147116.

31. Mata, M., Gerken, C., Nguyen, P., Krenciute, G., Spencer, D.M., and Gottschalk, S. (2017). Inducible Activation of MyD88 and CD40 in CAR T Cells Results in Controllable and Potent Antitumor Activity in Preclinical Solid Tumor Models. Cancer Discov. *7*, 1306–1319. https://doi.org/10.1158/2159-8290.CD-17-0263.

32. Starr, C.G., and Tessier, P.M. (2019). Selecting and engineering monoclonal antibodies with drug-like specificity. Curr. Opin. Biotechnol. *60*, 119–127. https://doi.org/10.1016/j.copbio.2019.01.008.

33. Golfier, S., Kopitz, C., Kahnert, A., Heisler, I., Schatz, C.A., Stelte-Ludwig, B., Mayer-Bartschmid, A., Unterschemmann, K., Bruder, S., Linden, L., et al. (2014). Anetumab ravtansine: a novel mesothelin-targeting antibody-drug conjugate cures tumors with heterogeneous target expression favored by bystander effect. Mol. Cancer Ther. *13*, 1537–1548. https://doi.org/10.1158/1535-7163.MCT-13-0926.

34. Tang, Y., and Cao, Y. (2020). Modeling the dynamics of antibody-target binding in living tumors. Sci. Rep. *10*, 16764. https://doi.org/10.1038/s41598-020-73711-y.

35. Baghban, R., Roshangar, L., Jahanban-Esfahlan, R., Seidi, K., Ebrahimi-Kalan, A., Jaymand, M., Kolahian, S., Javaheri, T., and Zare, P. (2020). Tumor microenvironment complexity and therapeutic implications at a glance. Cell Commun. Signal. *18*, 59. https://doi.org/10.1186/s12964-020-0530-4.

36. Nessler, I., Khera, E., Vance, S., Kopp, A., Qiu, Q., Keating, T.A., Abu-Yousif, A.O., Sandal, T., Legg, J., Thompson, L., et al. (2020). Increased Tumor Penetration of Single-Domain Antibody-Drug Conjugates Improves In Vivo Efficacy in Prostate Cancer Models. Cancer Res. *80*, 1268–1278. https://doi.org/10.1158/0008-5472.CAN-19-2295.

37. Wu, Y., Li, Q., Kong, Y., Wang, Z., Lei, C., Li, J., Ding, L., Wang, C., Cheng, Y., Wei, Y., et al. (2022). A highly stable human single-domain antibody-drug conjugate exhibits superior penetration and treatment of solid tumors. Mol. Ther. *30*, 2785–2799. https://doi.org/10.1016/j.ymthe.2022.04.013.

38. Rottey, S., Clarke, J., Aung, K., Machiels, J.P., Markman, B., Heinhuis, K.M., Millward, M., Lolkema, M., Patel, S.P., de Souza, P., et al. (2022). Phase I/IIa Trial of BMS-986148, an Anti-mesothelin Antibody-drug Conjugate, Alone or in Combination with Nivolumab in Patients with Advanced Solid Tumors. Clin. Cancer Res. *28*, 95–105. https://doi.org/10.1158/1078-0432.CCR-21-1181.

39. Kindler, H.L., Novello, S., Bearz, A., Ceresoli, G.L., Aerts, J.G.J.V., Spicer, J., Taylor, P., Nackaerts, K., Greystoke, A., Jennens, R., et al. (2022). Anetumab ravtansine versus vinorelbine in patients with relapsed, mesothelin-positive malignant pleural mesothelioma (ARCS-M): a randomised, open-label phase 2 trial. Lancet Oncol. *23*, 540–552. https://doi.org/10.1016/S1470-2045(22)00061-4.

40. Weekes, C.D., Lamberts, L.E., Borad, M.J., Voortman, J., McWilliams, R.R., Diamond, J.R., de Vries, E.G.E., Verheul, H.M., Lieu, C.H., Kim, G.P., et al. (2016). Phase I Study of DMOT4039A, an Antibody-Drug Conjugate Targeting Mesothelin, in Patients with Unresectable Pancreatic or Platinum-Resistant Ovarian Cancer. Mol. Cancer Ther. *15*, 439–447. https://doi.org/10.1158/1535-7163.MCT-15-0693.

41. Meyer, S., Evers, M., Jansen, J.H.M., Buijs, J., Broek, B., Reitsma, S.E., Moerer, P., Amini, M., Kretschmer, A., Ten Broeke, T., et al. (2018). New insights in Type I and II CD20 antibody mechanisms-of-action with a panel of novel CD20 antibodies. Br. J. Haematol. *180*, 808–820. https://doi.org/10.1111/bjh.15132.

42. Schneider, D., Xiong, Y., Wu, D., Hu, P., Alabanza, L., Steimle, B., Mahmud, H., Anthony-Gonda, K., Krueger, W., Zhu, Z., et al. (2021). Trispecific CD19-CD20-CD22-targeting duoCAR-T cells eliminate antigen-heterogeneous B cell tumors in preclinical models. Sci. Transl. Med. *13*, eabc6401. https://doi.org/10.1126/scitranslmed.abc6401.

43. Li, J.Y., Perry, S.R., Muniz-Medina, V., Wang, X., Wetzel, L.K., Rebelatto, M.C., Hinrichs, M.J.M., Bezabeh, B.Z., Fleming, R.L., Dimasi, N., et al. (2016). A Biparatopic HER2-Targeting Antibody-Drug Conjugate Induces Tumor Regression in Primary Models Refractory to or Ineligible for HER2-Targeted Therapy. Cancer Cell *29*, 117–129. https://doi.org/10.1016/j.ccell.2015.12.008.

44. Mansilla-Soto, J., Eyquem, J., Haubner, S., Hamieh, M., Feucht, J., Paillon, N., Zucchetti, A.E., Li, Z., Sjöstrand, M., Lindenbergh, P.L., et al. (2022). HLA-independent T cell receptors for targeting tumors with low antigen density. Nat. Med. *28*, 345–352. https://doi.org/10.1038/s41591-021-01621-1.

45. Anthony-Gonda, K., Bardhi, A., Ray, A., Flerin, N., Li, M., Chen, W., Ochsenbauer, C., Kappes, J.C., Krueger, W., Worden, A., et al. (2019). Multispecific anti-HIV duoCAR-T cells display broad in vitro antiviral activity and potent in vivo elimination of HIV-infected cells in a humanized mouse model. Sci. Transl. Med. *11*, eaav5685. https://doi.org/10.1126/scitranslmed.aav5685.

46. Fan, J., Zhuang, X., Yang, X., Xu, Y., Zhou, Z., Pan, L., and Chen, S. (2021). A multivalent biparatopic EGFR-targeting nanobody drug conjugate displays potent anticancer activity in solid tumor models. Signal Transduct. Target. Ther. *6*, 320. https://doi.org/10.1038/s41392-021-00666-5.

47. Pegram, M.D., Hamilton, E.P., Tan, A.R., Storniolo, A.M., Balic, K., Rosenbaum, A.I., Liang, M., He, P., Marshall, S., Scheuber, A., et al. (2021). First-in-Human, Phase 1 Dose-Escalation Study of Biparatopic Anti-HER2 Antibody-Drug Conjugate MEDI4276 in Patients with HER2-positive Advanced Breast or Gastric Cancer. Mol. Cancer Ther. *20*, 1442–1453. https://doi.org/10.1158/1535-7163.MCT-20-0014.

48. Chen, S.H., Hung, W.C., Wang, P., Paul, C., and Konstantopoulos, K. (2013). Mesothelin binding to CA125/MUC16 promotes pancreatic cancer cell motility and invasion via MMP-7 activation. Sci. Rep. *3*, 1870. https://doi.org/10.1038/srep01870.

49. Tomar, S., Zhang, J., Khanal, M., Hong, J., Venugopalan, A., Jiang, Q., Sengupta, M., Miettinen, M., Li, N., Pastan, I., et al. (2022). Development of Highly Effective Anti-Mesothelin hYP218 Chimeric Antigen Receptor T Cells With Increased Tumor Infiltration and Persistence for Treating Solid Tumors. Mol. Cancer Ther. *21*, 1195–1206. https://doi.org/10.1158/1535-7163.MCT-22-0073.

50. Liu, X., Onda, M., Watson, N., Hassan, R., Ho, M., Bera, T.K., Wei, J., Chakraborty, A., Beers, R., Zhou, Q., et al. (2022). Highly active CAR T cells that bind to a juxtamembrane region of mesothelin and are not blocked by shed mesothelin. Proc. Natl. Acad. Sci. USA *119*, e2202439119. https://doi.org/10.1073/pnas.2202439119.

51. Xiao, Q., Zhang, X., Tu, L., Cao, J., Hinrichs, C.S., and Su, X. (2022). Size-dependent activation of CAR-T cells. Sci. Immunol. *7*, eabl3995. https://doi.org/10.1126/sciimmunol.abl3995.

52. Xu, J., Chen, L.J., Yang, S.S., Sun, Y., Wu, W., Liu, Y.F., Xu, J., Zhuang, Y., Zhang, W., Weng, X.Q., et al. (2019). Exploratory trial of a biepitopic CAR T-targeting B cell maturation antigen in relapsed/refractory multiple myeloma. Proc. Natl. Acad. Sci. USA *116*, 9543–9551. https://doi.org/10.1073/pnas.1819745116.

53. Ma, J., Tang, W.K., Esser, L., Pastan, I., and Xia, D. (2012). Characterization of crystals of an antibody-recognition fragment of the cancer differentiation antigen mesothelin in complex with the therapeutic antibody MORAb-009. Acta Crystallogr. Sect. F Struct. Biol. Cryst. Commun. *68*, 950–953. https://doi.org/10.1107/S1744309112028229.

54. Suzuki, M., Roy, R., Zheng, H., Woychik, N., and Inouye, M. (2006). Bacterial bioreactors for high yield production of recombinant protein. J. Biol. Chem. *281*, 37559–37565. https://doi.org/10.1074/jbc.M608806200.

55. Emsley, P., and Cowtan, K. (2004). Coot: model-building tools for molecular graphics. Acta Crystallogr. D Biol. Crystallogr. *60*, 2126–2132. https://doi.org/10.1107/S0907444904019158.

56. Liebschner, D., Afonine, P.V., Baker, M.L., Bunkóczi, G., Chen, V.B., Croll, T.I., Hintze, B., Hung, L.W., Jain, S., McCoy, A.J., et al. (2019). Macromolecular structure determination using X-rays, neutrons and electrons: recent developments in Phenix. Acta Crystallogr. D Struct. Biol. *75*, 861–877. https://doi.org/10.1107/S2059798319011471.